Reduction of Near-Inertial Energy Through the Dependence of Wind Stress on the Ocean-Surface Velocity

Willi Rath[1], Richard J. Greatbatch[1], Xiaoming Zhai[2]

Corresponding author: Willi Rath, GEOMAR Helmholtz Centre for Ocean Research Kiel, Duesternbrooker Weg 20, D-24105 Kiel, Germany. (wrath@geomar.de)

[1]GEOMAR Helmholtz Centre for Ocean Research Kiel, Kiel, Germany.

[2]School of Environmental Sciences, University of East Anglia, Norwich, UK.

Abstract. A realistic primitive-equation model of the Southern Ocean at eddying spatial resolution is used to examine the effect of ocean-surface-velocity dependence of the wind stress on the strength of near-inertial oscillations. Accounting for the ocean-surface-velocity dependence of the wind stress leads to a large reduction of wind-induced near-inertial energy of approximately 40 percent and of wind power input into the near-inertial frequency band of approximately 20 percent. A large part of this reduction can be explained by the leading-order modification to the wind stress if the ocean-surface velocity is included. The strength of the reduction is shown to be modulated by the inverse of the ocean-surface-mixed-layer depth. We conclude that the effect of surface-velocity dependence of the wind stress should be taken into account when estimating the wind-power input into the near-inertial frequency band and when estimating near-inertial energy levels in the ocean due to wind forcing.

1. Introduction

Near-inertial oscillations (NIO) dominate the internal-wave spectrum of the ocean (see *Kunze* [1985]). They are thought to be a source for the energy that drives the meridional-overturning circulation (see *Munk and Wunsch* [1998]) and play a role in setting the surface-mixed-layer depth (see *Pollard et al.* [1972]) and thereby influence the sea-surface temperature (SST) with potentially important implications for climate (*Jochum et al.* [2012]). In the surface-mixed layer, NIOs are quasi-free horizontal motions that are typically generated by fast changes of the wind stress vector (*Pollard and Millard* [1970]; *Gill* [1982]). Once excited, NIOs are subject to deflection by the Coriolis force, dissipation (including the loss of kinetic energy to potential energy through entrainment of water into the mixed layer), stresses at the base of the mixed layer due the ambient flow field and propagation of near-inertial waves (NIW) out of the mixed layer (see, for example, *Gill* [1982], *Gill* [1984], *Plueddemann and Farrar* [2006], *Furuichi et al.* [2008], and *Zhai et al.* [2009]).

Our knowledge of wind power input (WPI) into the near-inertial frequency band, and also near-inertial energy (NIE) levels in the ocean, is only loosely constrained by observations. There are observational studies which have contributed to our understanding of the physics of NIOs by analyzing local observational data mainly from moorings (see *Pollard and Millard* [1970], *D'Asaro* [1985] and *Plueddemann and Farrar* [2006]), but it is only recently that the first direct estimates of global scale NIE have been obtained based on surface-drifter data (see *Elipot and Lumpkin* [2008] and *Chaigneau et al.* [2008]). In the meantime, the simple slab-ocean model proposed by *Pollard and Millard* [1970], described

in detail in Section 2.3, has been used to assess NIE and near-inertial WPI on a global scale (see *Watanabe and Hibiya* [2002], *Alford* [2003]). Moreover, it can be expected that numerical models will continue to be widely used in the future for assessing NIE and near-inertial WPI.

This study aims at understanding how including the ocean-surface velocity into the parameterization of the wind stress (called surface-velocity dependence, or SVD, hereafter) influences the levels of NIE in the surface-mixed layer and the near-inertial WPI. SVD is known to lead to a general damping of the ocean currents (see *Dewar and Flierl* [1987]) which can improve the modelled SST in climate models (see *Pacanowski* [1987] and *Luo et al.* [2005]). SVD has been shown to reduce WPI into geostrophic motions by up to 30% (see *Duhaut and Straub* [2006] and *Hughes and Wilson* [2008]) and mesoscale eddy kinetic energy (EKE) in a regional ocean model by about 10% (see *Zhai and Greatbatch* [2007]). The large effect of SVD on WPI into the large-scale circulation of the ocean suggests that SVD can also have a significant effect on NIE and WPI into the inertial frequency band.

As the main model to assess the relevance of SVD for NIOs, we use a realistic primitive-equation model at eddying resolution (SPFLAME). We find that SVD reduces temporally and horizontally averaged near-inertial WPI by as much as 34.5 % and temporally and horizontally averaged NIE by as much as 43.1 % in summer. Averaged over a whole year, horizontally averaged near-inertial WPI is reduced by 22.1 %, and horizontally averaged NIE is reduced by 39.9 % (see Table 1). We argue that a large part of the reduction can be explained by the leading-order correction to WPI induced by SVD. To illustrate the mechanism, we use the linear slab-ocean model of *Pollard and Millard* [1970] (hereafter

PM70). In PM70, SVD corresponds, to leading order, to adding a linear damping term to the momentum equation. The magnitude of the extra damping term is found to be set by the wind speed and the inverse of the mixed-layer depth.

In Section 2, we discuss the wind-stress parameterizations, and the models and experiments used in this study. In Section 3, we briefly describe the spatial and temporal distribution of NIE and near-inertial WPI in the primitive-equation model. Section 4 covers the main results of this study. First, we describe the large reduction of NIE and near-inertial WPI found in the primitive-equation-model experiments when including SVD. We then propose a simple mechanism that explains the observed reduction and show results from the slab-ocean model to confirm that a large reduction of NIE can be explained by the direct effect of the changed wind-stress parameterization. Finally, we show that the reduction of NIE and near-inertial WPI closely follow the annual cycle of the mixed-layer depth. Section 5 concludes with a summary. In the appendices, we briefly discuss the definition used for the mixed-layer depth, the time-filtering used to extract the near-inertial signal from the model output and the tuning of the slab-ocean model.

2. Methods, Models and Experiments

2.1. The Wind-Stress Parameterization

Conventionally, the wind stress is parameterized in terms of 10-m-wind speed, $\boldsymbol{U}_{10}$, alone. In terms of density of air close to the sea surface, ρ_a, and the drag coefficient, c_d, the wind stress is then defined as

$$\boldsymbol{\tau}_{CTL} \equiv \rho_a c_d(|\boldsymbol{U}_{10}|)|\boldsymbol{U}_{10}|\boldsymbol{U}_{10} \tag{1}$$

We chose to parameterize the drag coefficient according to *Large and Pond* [1981] with a leveling off for high wind speeds according to *Donelan et al.* [2004]. With the above parameterization of the wind stress, wind power input WPI is proportional to the projection of the wind-stress vector onto the ocean-surface-velocity vector $\boldsymbol{u}_o$

$$WPI_{CTL} \equiv \tau_{CTL} \cdot \boldsymbol{u}_o = \rho_a c_d(|\boldsymbol{U}_{10}|)|\boldsymbol{U}_{10}|\boldsymbol{U}_{10} \cdot \boldsymbol{u}_o \tag{2}$$

Alternatively, the wind stress can be parameterized in terms of the relative velocity of the wind and the ocean $\boldsymbol{U}_{10} - \boldsymbol{u}_o$

$$\boldsymbol{\tau}_{SVD} \equiv \rho_a c_d(|\boldsymbol{U}_{10} - \boldsymbol{u}_o|)|\boldsymbol{U}_{10} - \boldsymbol{u}_o|(\boldsymbol{U}_{10} - \boldsymbol{u}_o) \tag{3}$$

Duhaut and Straub [2006] show that the leading-order effect of changing the wind stress to $\boldsymbol{\tau}_{SVD}$ is

$$\Delta WPI \equiv WPI_{SVD} - WPI_{CTL} \approx -\rho_a c_d|\boldsymbol{U}_{10}|[|\boldsymbol{u}_o|^2 + (\boldsymbol{u}_o \cdot \hat{\boldsymbol{U}}_{10})^2] \tag{4}$$

where $\hat{\boldsymbol{U}}_{10}$ is the unit vector pointing in the direction of the 10-m-wind vector $\boldsymbol{U}_{10}$. Since both $|\boldsymbol{u}_o|^2$ and $(\boldsymbol{u}_o \cdot \hat{\boldsymbol{U}}_{10})^2$ are positive definite, the effect of SVD is a general reduction of WPI. This negative definite ΔWPI has been shown to provide a sink term for mesoscale EKE by *Zhai and Greatbatch* [2007].

2.2. A Realistic Primitive-Equation Model – SPFLAME

We use an eddying $(1/10)^\circ$ primitive-equation ocean model with realistic topography, as described by *Eden* [2006]. It covers the Southern Ocean between $78^\circ S$ and $30^\circ S$. In the vertical, the domain is separated into 42 levels with increasing thickness ranging from $10\,m$ at the surface to $250\,m$ at $5500\,m$ depth. The model is driven by six-hourly $10\,m$-winds from the ERA40 reanalysis (*Uppala et al.* [2005]) and by climatological surface-heat fluxes (see *Barnier et al.* [1995]). Surface salinity is restored to climatological values taken from

Levitus et al. [1994] with a time scale of 15 $days$ for the upper level of thickness 10 m. The surface-momentum flux is derived from 10m-winds using the two different wind-stress parameterizations given by (1) and (3) above. Vertical mixing is parameterized using the TKE-mixing scheme as described by *Gaspar et al.* [1990] and *Blanke and Delecluse* [1993], and horizontal mixing is parameterized in both the momentum and tracer equation as a biharmonic diffusivity. At $30°S$, an open boundary is used where barotropic in- and outflow are prescribed and where potential temperature and salinity are restored to climatological values.

The model has realistic levels of mesoscale EKE (see *Eden* [2006] for a comparison with an observational estimate of the EKE based on satellite altimetry). The modelled depth-integrated transport through Drake Passage of about 120 Sv is within the error bar of the estimate 134 ± 27 Sv given by *Cunningham et al.* [2003].

The model is spun up from rest (SPINUP-GCM) using the climatology of *Levitus et al.* [1994] (for salinity) and *Levitus and Boyer* [1994] (for potential temperature) as the initial condition and using the conventional parameterization of the wind stress (see equation (1)) for 31 years. The years 1 to 10 of the spin-up phase are forced by climatological wind stress, and the years 11 to 31 are forced by conventional wind stress, given by (1), for the years 1980 to 2000 of 6-hourly 10-m-wind fields from the ERA40 reanalysis. Then, the experiment is forked into two runs, one of which continues to be forced by conventional wind stress (equation (1)), and one of which is forced by surface-velocity-dependent wind stress (equation (3)). We name these two runs CONTROL-GCM and SVD-GCM respectively. Note that we start the analysis of the two model runs immediately after the forking and that, consequently, the adjustment of the run SVD-GCM to the new wind-

stress parameterization is contained in the data we analyze. The mesoscale-eddy field is important in modulating the small-scale structure of the spatial distribution of NIE by locally changing the effective Coriolis parameter (see *Zhai et al.* [2005], *Zhai et al.* [2007]). Adjustment of the run SVD-GCM to the new wind stress parameterization involves the model switching into a different realization of the (chaotic) mesoscale-eddy field. To be sure to capture the direct effect of the changed wind stress parameterization rather than a secondary effect due to a changed mesoscale, we decided to accept the disadvantage of a run that is subject to adjustment. We discuss the implications of the adjustment process for our results in Section 4, where we also note that NIE itself goes through an adjustment process to the change in the wind-stress parameterization.

The first 36.5 days of the output from the runs CONTROL-GCM and SVD-GCM are available at a high spatial resolution ($1/10^\circ \times 1/10^\circ$) and at a high temporal resolution (3 hours). For the rest of the runs CONTROL-GCM and SVD-GCM, covering the year 2001, we reduced the spatial resolution of the model output to $1^\circ \times 1^\circ$ without changing the temporal resolution. By comparing the full-resolution output for the first 36.5 days to the reduced-resolution output over the same period, we found that NIE at the reduced-resolution contains all the information that is relevant for this study, and hence decided to use the $1^\circ \times 1^\circ$ resolution output throughout.

To calculate NIE, we filtered the velocity field to near-inertial frequencies by using a fifth-order Butterworth filter as described in Appendix B. Throughout the manuscript, the subscript I indicates near-inertially filtered quantities.

2.3. A Linear Slab-Ocean Model – PM70

Pollard and Millard [1970] proposed a local linear slab-ocean model for near-inertial oscillations (PM70) which has since been widely used to assess the input of near-inertial energy into the surface-mixed layer of the ocean (*Alford* [2003]). It is a local model for the near-inertial velocity in the mixed layer (u, v) featuring the Coriolis force $f(-v, u)$, the wind stress $\boldsymbol{\tau} = (\tau^x, \tau^y)$, a linear damping term with the coefficient ϵ, the mixed-layer depth H (assumed to be time-independent), and the reference density ρ_0:

$$u_t - fv = \frac{\tau^x}{\rho_0 H} - \epsilon u \tag{5}$$

$$v_t + fu = \frac{\tau^y}{\rho_0 H} - \epsilon v \tag{6}$$

The time-evolution of kinetic energy, $E = \boldsymbol{u} \cdot \boldsymbol{u}/2$, in PM70 is governed by

$$E_t = uu_t + vv_t = \frac{1}{\rho_0 H}(\tau^x u + \tau^y v) - \epsilon(u^2 + v^2) \tag{7}$$

To numerically integrate the slab model, we chose to discretize the Coriolis term with centered differences, and the explicit linear damping, as well as the wind-stress term using a backward scheme. For the surface-velocity-dependent case, the wind-forcing term includes a damping component that can become unstable if it is discretized with centered differences.

The model is started from rest. We prescribe a spatially varying mixed-layer depth that has been diagnosed from the initial 36.5 days of the experiment CONTROL-GCM as described in Appendix A, and use the same 6-hourly-wind fields used to drive the primitive-equation model in the initial 36.5 days of the experiments CONTROL-GCM and SVD-GCM. We call the experiments CONTROL-SLAB (with conventional wind stress) and SVD-SLAB (with surface-velocity-dependent wind stress). The only free parameter of the model is then the explicit linear-damping time scale $1/\epsilon$ which we set to 4.5 days

for both the experiments CONTROL-SLAB and SVD-SLAB. For details on the tuning of ϵ, we refer to Appendix C. The velocity fields from the PM70 experiments are filtered using the same filter as for the SPFLAME data (see Appendix B).

3. Near-Inertial Energy in an Eddying Model of the Southern Ocean

Figures 1 a,b and 2 a,b show NIE in the mixed layer for the primitive-equation-model experiments CONTROL-GCM and SVD-GCM time-averaged for January 2001 and for the whole year 2001. North of approximately $55°S$, high levels of mixed-layer NIE ($200\,\mathrm{J/m^2}$ and more) are concentrated in patches of a few degrees in diameter. South of approximately $55°S$ low levels of mixed-layer NIE ($100\,\mathrm{J/m^2}$ and less) prevail and spots of high NIE are completely absent. Figures 3 a,b and 4 a,b show near-inertial WPI for CONTROL-GCM and SVD-GCM time-averaged for January 2001 and for the whole year 2001. As for NIE, high levels of near-inertial WPI (above $1\mathrm{mWm^{-2}}$) occur in relatively small patches. For a detailed examination of the spatial and temporal distribution of NIE and near-inertial WPI in the Southern Ocean, we refer to the companion paper *Rath et al.* [2013]. *Rath et al.* [2013] explain the concentration of high NIE and near-inertial WPI at latitudes that are most of the time significantly north of the Southern Hemisphere storm track by the joint effect of a shallow mixed-layer depth north of the ACC, and a reduced near-inertial variability of the wind stress at high latitudes due to the increase in the magnitude of the Coriolis parameter at high latitudes.

Figure 5 a shows temporally and horizontally averaged NIE from the experiments CONTROL-GCM and SVD-GCM for January 2001 and for the whole year 2001. NIE is concentrated at the surface. In January, when the mixed-layer depth is close to its annual

minimum, high NIE is confined to depths less than 100 m. In the whole-year average, high horizontally averaged NIE reaches down to approximately 200 m.

4. Influence of the Ocean-Surface-Velocity Dependence of the Wind-Stress on the Near-Inertial Frequency Band

In this section, we first report a large reduction of temporally averaged mixed-layer NIE and near-inertial WPI due to SVD in the primitive-equation-model experiments CONTROL-GCM and SVD-GCM. We then propose a simple meachanism by which the leading-order correction to the wind-stress leads to a reduction of NIE and near-inertial WPI approximately proportional to the inverse of the mixed-layer depth. We test this mechanism by showing that the PM70 slab-ocean model largely captures the reduction of mixed-layer NIE, and by showing that the annual cycle of the reduction is closely tied to the annual cycle of the inverse of the mixed-layer depth.

4.1. SPFLAME

When comparing the levels of mixed-layer NIE and of near-inertial WPI in the experiments CONTROL-GCM (See Figure 1 a and Figure 2 a, and Figure 3 a and Figure 4 a respectively.) and in the experiment SVD-GCM (See Figure 1 b and Figure 2 b, and Figure 3 b and Figure 4 b respectively.), the most striking difference is the large reduction if the surface-velocity-dependent wind stress is used. To quantify the reduction, we define the relative differences of NIE, R_{NIE}, and of near-inertial WPI, R_{WPI}, as

$$R_{NIE} \equiv \frac{E_I|_{SVD} - E_I|_{CTL}}{E_I|_{CTL}} \tag{8}$$

$$R_{WPI} \equiv \frac{WPI_I|_{SVD} - WPI_I|_{CTL}}{WPI_I|_{CTL}}. \tag{9}$$

Figure 1 c and Figure 2 c show the relative reduction of time-averaged mixed-layer NIE for January 2001 and for the whole year 2001 together with isolines of the time-averaged mixed-layer depth. The largest reduction (more than 60% in the South Pacific) occurs in January where the mixed layer is shallow. The relative reduction of near-inertial WPI is shown in Figure 3 c and Figure 4 c. Again, the largest reduction occurs north of the ACC, when the mixed-layer is shallow. Along the ACC, where the mixed layer is deep, and where a vigorous mesoscale-eddy field is present, the relative reduction of NIE and near-inertial WPI are much smaller.

Table 1 lists temporally and horizontally averaged mixed-layer NIE, temporally averaged and horizontally integrated near-inertial WPI, and the relative differences thereof, R_{NIE} and R_{WPI}, for January 2001 and for the whole year 2001. Mixed-layer NIE is reduced by 43.1 % in January 2001 (39.9 % for the whole year), and near-inertial WPI is reduced by 34.5 % in January 2001 (22.1 % for the whole year).

The horizontally averaged view presented in Figure 5 shows a large reduction of NIE, which extends to all depths. For January 2001, the relative reduction of NIE is biggest close to the surface and then decays to lower values for greater depths. If the averaging period is extended to the whole year 2001, the reduction of temporally and horizontally averaged NIE is largely uniform throughout the water column. The difference between the average over the whole year, and over only January, indicates that NIE at depth is fed from the NIE that the wind injects at the surface and which in turn spreads to depth from above, as discussed further below.

SVD-GCM is subject to an adjustment to the new wind-stress parameterization. We expect, that in January 2001, when the information about the reduction of NIE at the

surface has not yet been transferred to all depths, that the reduction of NIE in the deep ocean is underestimated. Figure 7 a, to be discussed in detail later, shows that the mixed-layer NIE is adjusting relatively quickly, while it takes approximately a month before the information about the reduction of the NIE that is injected at the surface reaches the deep ocean. Note that the temporal evolution of horizontally averaged NIE is an integral over many bursts of NIOs in different locations with different mixed-layer depths and hence does not necessarily allow for an estimate of the rate at which NIE is transferred to the deep ocean locally.

4.2. Mechanism for Reducing Near-Inertial Energy by Surface-Velocity-Dependent Wind Stress

In the framework of the simple slab-ocean model PM70 (see Section 2 for details), the difference of the PM70 wind-stress terms leads to a difference of the wind-power-input term of the energy equation (4) that is proportional to the wind speed $|\boldsymbol{U}_{10}|$ and to the energy:

$$\frac{\Delta WPI}{\rho_0 H} = -\frac{\rho_a c_d}{\rho_0 H}[1 + (\hat{\boldsymbol{u}}_o \cdot \hat{\boldsymbol{U}}_{10})^2]|\boldsymbol{U}_{10}||\boldsymbol{u}_o|^2 = -\epsilon_{SVD}|\boldsymbol{u}_o|^2 \tag{10}$$

where

$$\epsilon_{SVD} \equiv \frac{\rho_a c_d}{\rho_0 H}[1 + (\hat{\boldsymbol{u}}_o \cdot \hat{\boldsymbol{U}}_{10})^2]|\boldsymbol{U}_{10}| \tag{11}$$

with $\hat{\boldsymbol{u}}_o = \boldsymbol{u}_o/|\boldsymbol{u}_o|$. To leading order, the difference of WPI acts like an extra linear-damping term with the damping time scale $1/\epsilon_{SVD}$. It should be noted that the derivation of (10) and (11) includes two strong assumptions: The mixed-layer depth, H, has been assumed to be time-independent and also the same, irrespective of whether the wind stress contains the SVD or not.

Consider a freely decaying near-inertial oscillation that is only subject to linear damping. The time-integral of NIE is then proportional to the inverse of the linear-damping coefficient. Let $\tilde{\epsilon} = \epsilon + \epsilon_{SVD}$. Then, for the same initial conditions, the relative difference, R_{NIE}, of NIE subject to damping with ϵ alone, compared to damping with $\tilde{\epsilon}$, is $\epsilon_{SVD}/(\epsilon+\epsilon_{SVD})$. If the linear damping due to SVD is of the same size as the linear damping modelling all other processes that remove NIE from the mixed layer, NIE is reduced by 50 %.

The term $(\hat{\boldsymbol{u}}_o \cdot \hat{\boldsymbol{U}}_{10})^2$ vanishes if the wind vector is orthogonal to the ocean-velocity vector and is one if the wind vector and the ocean-velocity vector are exactly (anti-)parallel. If the relative direction of the wind vector and the ocean-velocity vector is completely random, $(\hat{\boldsymbol{u}}_o \cdot \hat{\boldsymbol{U}}_{10})^2$ is a Monte-Carlo estimator for $\int_0^{2\pi} \mathrm{d}x \cos^2 x = 0.5$. With $\rho_a = 1.22\,\mathrm{kgm}^{-3}$, $\rho_0 = 1035\,\mathrm{kgm}^{-3}$, $c_d \approx 1.2 \cdot 10^{-3}$, and $(\hat{\boldsymbol{u}}_o \cdot \hat{\boldsymbol{U}}_{10})^2 \approx 0.5$, the linear-damping due to SVD acts on time scales similar to

$$\frac{1}{\epsilon_{SVD}} \approx 5\,\mathrm{days}\,\frac{H}{|\boldsymbol{U}_{10}|}\mathrm{s}^{-1}. \tag{12}$$

For typical wind speeds around $10\,\mathrm{ms}^{-1}$ the extra damping associated with surface-velocity dependence of the wind stress acts on a timescale of approximately 25 days for $H \approx 50\,\mathrm{m}$ and on a time scale of approximately 5 days for $H \approx 10\,\mathrm{m}$. Earlier studies using PM70 such as that by *D'Asaro* [1985] or *Pollard and Millard* [1970] found a linear-damping time scale, $1/\epsilon$, of 1 to 10 days to be appropriate for modelling observed time series of near-inertial velocity. Hence, with a shallow mixed layer, or with strong winds, ϵ_{SVD} may compete with the other processes that remove NIE from the mixed layer (and, indeed, may be included in the estimate for ϵ given by the above authors).

Plueddemann and Farrar [2006] found that shear instability at the base of the mixed layer is an important sink for NIE in the mixed layer. In SVD-GCM, the reduction in NIE compared to CONTROL-GCM, leads to less vertical shear across the base of the surface-mixed layer and hence less turbulent entrainment there. This rules out the possibility that the reduction of NIE in SVD-GCM is partly due to an increased efficiency of shear instability at the mixed-layer base.

4.3. Testing of the Proposed Mechanism for the Reduction of Near-Inertial Energy using PM70 – Summer Conditions

To test the hypothesis that the large reduction of near-inertial energy seen in the primitive-equation experiments can be explained by the direct effect of the changed wind stress, we use the PM70 slab-ocean model. We assume that there is a spatially and temporally universal linear-damping parameter, ϵ, (see equations (5) and (6)) that can be used to model the distribution of NIE in the Southern Ocean. This is a strong constraint, and, as pointed out by *Plueddemann and Farrar* [2006], a universal damping parameter is not sufficient for accurately modelling the time evolution of near-inertial currents for long time series. Note also that the choice of the spatial dependence of the linear damping parameter in PM70-like experiments is not agreed upon in the literature. *Alford* [2003] uses a damping coefficient which is proportional to f, while *Watanabe and Hibiya* [2002] use spatially uniform damping coefficients. Hence, we cannot expect the PM70 slab model to account for the spatial distribution of near-inertial energy and its reduction in detail. However, we will show that the broad spatial distribution as well as the magnitude of NIE and its reduction for surface-velocity-dependent wind stress can be captured by PM70.

In the following, we present the results from the experiments CONTROL-SLAB and SVD-SLAB and compare them to those of the experiments CONTROL-GCM and SVD-GCM. In order to isolate the effect of the wind stress parameterization, both PM70 experiments use an explicit damping $\epsilon = 1/4.5\,days$ everywhere. The tuning of the damping parameter is described in Appendix C. In order to test the effect of the change in the wind-stress parameterization, we also use a time-independent mixed-layer depth, H, although, importantly, H varies spatially and is the monthly mean for January diagnosed from CONTROL-GCM as described in Appendix A.

Figure 6 a and b show time-averaged mixed-layer NIE for the slab-model experiments. The spatial pattern of NIE in the SPFLAME runs (Figure 1) is largely reproduced. However the slab model fails to capture the much finer spatial structure seen in the primitive-equation-model output pointing to the relevance of the mesoscale-eddy field (see, e.g., *Zhai et al.* [2005], *Zhai et al.* [2007], and *Chavanne et al.* [2012]), which is neglected in the PM70 experiments.

Figure 6 c shows the relative difference of NIE in the slab-model experiments. There is a broad agreement between PM70 and SPFLAME in showing a large reduction of NIE where the mixed layer is shallow and in showing a small or no reduction where the mixed layer is deep, consistent with expectations from the mixed layer depth dependence in (12). It should be noted that there is disagreement in the spatial distribution of the relative reduction of NIE in the South Pacific between $65°S$ and $50°S$. In this region, the NIE reduction modelled by PM70 closely follows the mixed-layer depth, as expected, while the NIE reduction as measured from CONTROL-GCM and SVD-GCM is bigger than 65 % even where the mixed layer is relatively deep.

315 The simple slab-ocean model PM70 confirmed that including the ocean-surface velocity
316 in the parameterization of the wind-stress can directly reduce NIE in the mixed layer
317 by a large amount. Further, despite its simplicity, it is notable that PM70 even largely
318 captured the spatial distribution of the reduction, which, in turn, is controlled primarily
319 by the mixed layer depth.

4.4. The Annual Cycle

320 The mixed-layer depth is subject to a significant annual cycle. At the same location, the
321 mixed-layer depth can vary by an order of magnitude (see, e.g., Figure 5 in *de Boyer Mon-*
322 *tegut et al.* [2004]). From (12), we can expect the reduction of NIE and near-inertial WPI
323 associated with SVD to be tightly related to the annual cycle of the mixed-layer depth.

324 Figure 7 a shows the relative difference of horizontally averaged NIE, R_{NIE}, for the
325 upper 900 m of the water column. The reduction of NIE in the mixed layer is changing
326 from more than 50 % in austral summer, when the mixed-layer is shallow, to approximately
327 15 % in austral winter, when the mixed layer is deep. Figure 7 a also reveals that the
328 reduction of NIE injected at the surface causes a reduction of the levels of NIE in the
329 deep ocean as well. At the beginning of the time series, the adjustment of the experiment
330 SVD-GCM following the change in the wind-stress parameterization is clearly visible. For
331 horizontally averaged NIE, it takes approximately a month until the information about
332 the significant reduction of NIE injected at the surface is transferred to the deep ocean.

333 Figure 7 b and c show the zonally averaged reduction of mixed-layer NIE, R_{NIE}, and
334 of zonally averaged near-inertial WPI, R_{WPI}, together with the zonally averaged mixed-
335 layer depth. In austral summer, the large reduction reaches south to approximately $50°S$,
336 south of which the mixed-layer depth is considerably deeper than in the northern part of

the model domain. In fall, the deep mixed-layer expands towards the north and the region of the large reduction retreats accordingly, until in winter the reduction has reduced to its annual minimum. As the mixed-layer gets shallower in spring, the reduction recovers its largest extent again.

Figure 7 d summarizes Figure 7 a,b,c by showing that both, the reduction of horizontally averaged mixed-layer NIE, R_{NIE}, and the reduction of horizontally averaged near-inertial WPI closely follow the horizontally averaged mixed-layer depth, and that the annual minima and maxima of both almost exactly coincide with the annual maxima and minima of the mixed-layer depth.

5. Summary and Conclusion

We have used an eddying realistic primitive-equation model of the Southern Ocean to examine the relevance of the ocean-surface-velocity-dependence of the wind stress for determining NIE and for WPI into the near-inertial frequency band. We found a large reduction of both NIE and WPI into the near-inertial frequency band if the wind-stress parameterization accounts for the ocean-surface velocity. Averaged over the whole year, 2001, horizontally averaged mixed-layer NIE is reduced by 39.9 % and horizontally averaged WPI is reduced by 22.1 %. Locally, much larger reductions are found especially in the South Pacific. As NIE at depth in our model mainly feeds from NIE injected into the surface-mixed layer, there is a reduction of NIE all throughout the water column.

The reduction of NIE is due to the fact that including ocean-surface-velocity in the wind stress amounts, to leading order, to adding a linear-damping term to the momentum equation for the surface-mixed layer. This linear-damping term is proportional to the inverse of the mixed-layer depth. Using the slab-ocean model first described by *Pollard*

and Millard [1970], we confirmed that a large part of the observed reduction of near-inertial WPI and NIE can be explained by the direct effect of the changed wind-stress parameterization. By examining the annual cycle of NIE and the mixed-layer depth, we confirmed that it is in fact the inverse mixed-layer depth which mainly determines the strength of the reduction of NIE.

Our findings show that ocean-surface-velocity dependence of the wind stress has a big effect on wind-induced near-inertial oscillations and hence should be taken into account when WPI into the near-inertial frequency band is estimated.

Appendix A: The Mixed-Layer Depth

The mixed-layer depth used in this paper is defined as the depth at which the modulus of the deviation of the primitive-equation-model potential temperature to the surface temperature equals $\Delta T = 0.3\,\mathrm{K}$. ΔT has been chosen so that the mixed-layer depth approximately matches the depth at which the ratio $E_I(z)/E_I(0) \approx 1/e$ in regions with strong NIE, where $E_I(z)$ is the energy in the inertial frequency band at depth z. In the PM70 experiments, the mixed-layer depth, H, is taken to be the mean mixed-layer depth at each horizontal grid point over the month of January 2001. We compared different definitions for the mixed-layer depth and found that the results of this study are not significantly changed.

Appendix B: Time Filtering

The model output from the experiments CONTROL-GCM and SVD-GCM and from the corresponding PM70 experiments was filtered using a fifth-order Butterworth filter similar to the one used by *Zhai et al.* [2009]. We chose the cutoff frequencies to match the

Coriolis parameter f at the latitudes $28°S$ and $80°S$ which are just north and south of the boundaries of the model domain. Using the filter, the velocity was split into sub-inertial (S), near-inertial (I), and super-inertial (T) components

$$\boldsymbol{u} \equiv \boldsymbol{u}_S + \boldsymbol{u}_I + \boldsymbol{u}_T. \tag{B1}$$

Kinetic energy for each frequency band is then defined as

$$E_{S,I,T} \equiv \frac{u^2_{S,I,T} + v^2_{S,I,T}}{2} \tag{B2}$$

To avoid complications from the band-pass filter, which needs a couple of days data to be fully defined, we chose to neglect the first five and the last five days of the filtered data.

Appendix C: Tuning of the PM70 Experiment CONTROL-SLAB

Figure 8 compares the mixed-layer-averaged zonal near-inertial velocity from the experiment CONTROL-GCM and the zonal near-inertial velocity from PM70 at $100°E$ and $45°S$. PM70 is forced by the same wind-forcing as CONTROL-GCM, and is the same as used in CONTROL-SLAB. The mixed-layer depth from the experiment CONTROL-GCM $H = 36.1\,\mathrm{m}$ was used. The linear-damping parameter $\epsilon = 1/4.5\,\mathrm{days}$ was chosen by comparing PM70 output for different ϵ, and primitive-equation-model output from the experiment CONTROL-GCM. There are six to seven separate bursts of inertial oscillations and it is evident that PM70 does not capture the magnitude and shape of all of them.

Acknowledgments. WR and RJG thank the DFG for support under the grant *Influence of the ocean surface velocity dependence of the wind stress on the dynamics of the Southern Ocean*. Thanks also to GEOMAR for continuing support and to the University Computing Center of the University of Kiel. WR thanks Lars Czeschel and Carsten Eden

for providing initial help with the model. We thank Ryan Abernathey and an anonymous reviewer for their constructive comments that lead to a much improved manuscript.

References

Alford, M. (2003), Improved global maps and 54-year history of wind-work on ocean inertial motions, *Geophysical Research Letters*, *30*(8), doi:10.1029/2002GL016614.

Barnier, B., L. Siefridt, and P. Marchesiello (1995), Thermal Forcing for a global ocean circulation model using a 3-year climatology of ECMWF analyses, *Journal of Marine Systems*, *6*(4), 363–380, doi:10.1016/0924-7963(94)00034-9.

Blanke, B., and P. Delecluse (1993), Variability of the tropical Atlantic Ocean simulated by a general-circulation model with 2 different mixed-layer physics, *Journal of Physical Oceanography*, *23*(7), 1363–1388, doi:10.1175/1520-0485(1993)023.

Chaigneau, A., O. Pizarro, and W. Rojas (2008), Global climatology of near-inertial current characteristics from Lagrangian observations, *Geophysical Research Letters*, *35*(13), doi:10.1029/2008GL034060.

Chavanne, C. P., E. Firing, and F. Ascani (2012), Inertial Oscillations in Geostrophic Flow: Is the Inertial Frequency Shifted by zeta/2 or by zeta?, *JOURNAL OF PHYSICAL OCEANOGRAPHY*, *42*(5), 884–888, doi:10.1175/JPO-D-12-031.1.

Cunningham, S., S. Alderson, B. King, and M. Brandon (2003), Transport and variability of the Antarctic Circumpolar Current in Drake Passage, *Journal of Geophysical Research - Oceans*, *108*(C5), doi:10.1029/2001JC001147.

D'Asaro, E. (1985), The energy flux from the wind to near-inertial motions in the surface mixed layer, *Journal of Physical Oceanography*, *15*(8), 1043–1059, doi:10.1175/1520-

421 0485(1985)015.

422 de Boyer Montegut, C., G. Madec, A. Fischer, A. Lazar, and D. Iudicone (2004),
423 Mixed layer depth over the global ocean: An examination of profile data and a
424 profile-based climatology, *Journal of Geophysical Research - Oceans*, *109*(C12), doi:
425 10.1029/2004JC002378.

426 Dewar, W., and G. Flierl (1987), Some effects of the wind on rings, *Journal of Physical*
427 *Oceanography*, *17*(10), 1653–1667, doi:10.1175/1520-0485(1987)017.

428 Donelan, M., B. Haus, N. Reul, W. Plant, M. Stiassnie, H. Graber, O. Brown, and
429 E. Saltzman (2004), On the limiting aerodynamic roughness of the ocean in very strong
430 winds, *Geophysical Research Letters*, *31*(18), doi:10.1029/2004GL019460.

431 Duhaut, T., and D. Straub (2006), Wind stress dependence on ocean surface velocity: Im-
432 plications for mechanical energy input to ocean circulation, *Journal of Physical Oceanog-*
433 *raphy*, *36*(2), 202–211, doi:10.1175/JPO2842.1.

434 Eden, C. (2006), Thickness diffusivity in the Southern Ocean, *Geophysical Research Let-*
435 *ters*, *33*(11), doi:10.1029/2006GL026157.

436 Elipot, S., and R. Lumpkin (2008), Spectral description of oceanic near-surface variability,
437 *Geophysical Research Letters*, *35*(5), doi:10.1029/2007GL032874.

438 Furuichi, N., T. Hibiya, and Y. Niwa (2008), Model-predicted distribution of wind-induced
439 internal wave energy in the world's oceans, *Journal of Geophysical Research - Oceans*,
440 *113*(C9), doi:10.1029/2008JC004768.

441 Gaspar, P., Y. Gregoris, and J. Lefevre (1990), A simple eddy kinetic-energy model for
442 simulations of the oceanic vertical mixing - tests at Station Papa and Long-Term Upper
443 Ocean Study Site, *Journal of Geophysical Research - Oceans*, *95*(C9), 16,179–16,193,

444 doi:10.1029/JC095iC09p16179.

445 Gill, A. E. (1982), *Atmosphere-Ocean Dynamics*, Academic Press.

446 Gill, A. (1984), On the behavior of internal waves in the wakes of storms, *Journal of*
447 *Physical Oceanography*, *14*(7), 1129–1151.

448 Hughes, C. W., and C. Wilson (2008), Wind work on the geostrophic ocean circulation: An
449 observational study of the effect of small scales in the wind stress, *Journal of Geophysical*
450 *Research - Oceans*, *113*(C2), doi:10.1029/2007JC004371.

451 Jochum, M., B. P. Briegleb, G. Danabasoglu, W. G. Large, S. R. Jayne, M. H. Alford, and
452 F. O. Bryan (2012), On the impact of oceanic near-inertial waves on climate, *submitted*
453 *to Journal of Climate*.

454 Kunze, E. (1985), Near-inertial wave-propagation in geostrophic shear, *Journal of Physical*
455 *Oceanography*, *15*(5), 544–565, doi:10.1175/1520-0485(1985)015.

456 Large, W., and S. Pond (1981), Open Ocean Momentum Flux Measurements in Moderate
457 to Strong Winds, *Journal of Physical Oceanography*, *11*(3), 324–336, doi:10.1175/1520-
458 0485(1981)011.

459 Levitus, S., and T. Boyer (1994), World Ocean Atlas 1994. Volume 4: Temperature,
460 *NOAA Atlas NEDSIS 4*, NOAA, Washington D.C.

461 Levitus, S., R. Burgett, and T. Boyer (1994), World Ocean Atlas 1994. Volume 3: Salinity,
462 *NOAA Atlas NEDSIS 3*, NOAA, Washington D.C.

463 Luo, J., S. Masson, E. Roeckner, G. Madec, and T. Yamagata (2005), Reducing clima-
464 tology bias in an ocean-atmosphere CGCM with improved coupling physics, *Journal of*
465 *Climate*, *18*(13), 2344–2360, doi:10.1175/JCLI3404.1.

Munk, W., and C. Wunsch (1998), Abyssal recipes II: energetics of tidal and wind mixing, *Deep-Sea Research Part I-Oceanographic Research Papers*, *45*(12), 1977–2010, doi: 10.1016/S0967-0637(98)00070-3.

Pacanowski, R. (1987), Effect of equatorial currents on surface stress, *Journal of Physical Oceanography*, *17*(6), 833–838, doi:10.1175/1520-0485(1987)017.

Plueddemann, A., and J. Farrar (2006), Observations and models of the energy flux from the wind to mixed-layer inertial currents, *Deep-Sea Research Part II-Topical Studies in Oceanography*, *53*(1-2), 5–30, doi:10.1016/j.dsr2.2005.10.017.

Pollard, R., and R. Millard (1970), Comparison between observed and simulated wind-generated inertial oscillations, *Deep Sea Research and Oceanographic Abstracts*, *17*(4), 813 – 816, IN5, 817–821, doi:10.1016/0011-7471(70)90043-4.

Pollard, R. T., P. B. Rhines, and R. O. R. Y. Thompson (1972), The deepening of the wind-mixed layer, *Geophysical Fluid Dynamics*, *4*(1), 381–404, doi: 10.1080/03091927208236105.

Rath, W., R. Greatbatch, and Z. X (2013), On the spatial and temporal distribution of near-inertial energy and near-inertial wind power input in the Southern Ocean, *in preparation*.

Uppala, S., P. Kallberg, A. Simmons, U. Andrae, V. Bechtold, M. Fiorino, J. Gibson, J. Haseler, A. Hernandez, G. Kelly, X. Li, K. Onogi, S. Saarinen, N. Sokka, R. Allan, E. Andersson, K. Arpe, M. Balmaseda, A. Beljaars, L. Van De Berg, J. Bidlot, N. Bormann, S. Caires, F. Chevallier, A. Dethof, M. Dragosavac, M. Fisher, M. Fuentes, S. Hagemann, E. Holm, B. Hoskins, L. Isaksen, P. Janssen, R. Jenne, A. McNally, J. Mahfouf, J. Morcrette, N. Rayner, R. Saunders, P. Simon, A. Sterl, K. Trenberth,

A. Untch, D. Vasiljevic, P. Viterbo, and J. Woollen (2005), The ERA-40 re-analysis, *Quarterly Journal of the Royal Meteorological Society*, *131*(612, Part B), 2961–3012, doi:10.1256/qj.04.176.

Watanabe, M., and T. Hibiya (2002), Global estimates of the wind-induced energy flux to inertial motions in the surface mixed layer, *Geophysical Research Letters*, *29*(8), doi:10.1029/2001GL014422.

Zhai, X., R. Greatbatch, and J. Zhao (2005), Enhanced vertical propagation of storm-induced near-inertial energy in an eddying ocean channel model, *Geophysical Research Letters*, *32*(18), doi:10.1029/2005GL023643.

Zhai, X., and R. J. Greatbatch (2007), Wind work in a model of the northwest Atlantic Ocean, *Geophys. Res. Lett.*, *34*, doi:10.1029/2006GL028907.

Zhai, X., R. J. Greatbatch, and C. Eden (2007), Spreading of near-inertial energy in a 1/12 degrees model of the North Atlantic Ocean, *Geophysical Research Letters*, *34*(10), doi:10.1029/2007GL029895.

Zhai, X., R. J. Greatbatch, C. Eden, and T. Hibiya (2009), On the loss of wind-induced near-inertial energy to turbulent mixing in the upper ocean, *Journal of Physical Oceanography*, *39*, 3040–3045, doi:10.1175/2009JPO4259.1.

	Jan. 2001	whole 2001
NIE, CONTROL-GCM	$119.9\,\mathrm{Jm^{-2}}$	$135.8\,\mathrm{Jm^{-2}}$
NIE, SVD-GCM	$68.2\,\mathrm{Jm^{-2}}$	$82.9\,\mathrm{Jm^{-2}}$
R_{NIE}	$-43.1\,\%$	$-39.9\,\%$
WPI, CONTROL-GCM	$0.055\,\mathrm{TW}$	$0.068\,\mathrm{TW}$
WPI, SVD-GCM	$0.036\,\mathrm{TW}$	$0.053\,\mathrm{TW}$
R_{WPI}	$-34.5\,\%$	$-22.1\,\%$

Table 1. Temporally and horizontally averaged mixed-layer NIE and temporally averaged and horizontally integrated near-inertial WPI for the whole model domain together with the relative differences for the experiments CONTROL-GCM and SVD-GCM.

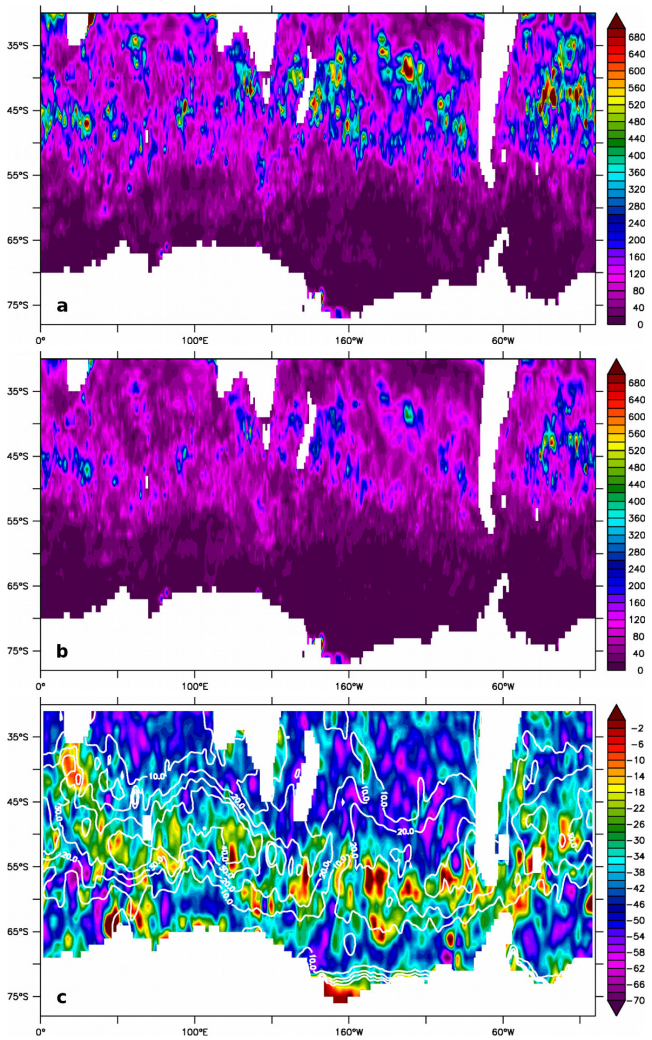

Figure 1. (a) CONTROL-GCM and (b) SVD-GCM time-averaged NIE integrated over the mixed layer (in Jm^{-2}) for January 2001. (c) Relative difference of the two (in %), as defined in (8), together with the 10, 20, 30, and 40 m contour lines of time-averaged mixed-layer depth.

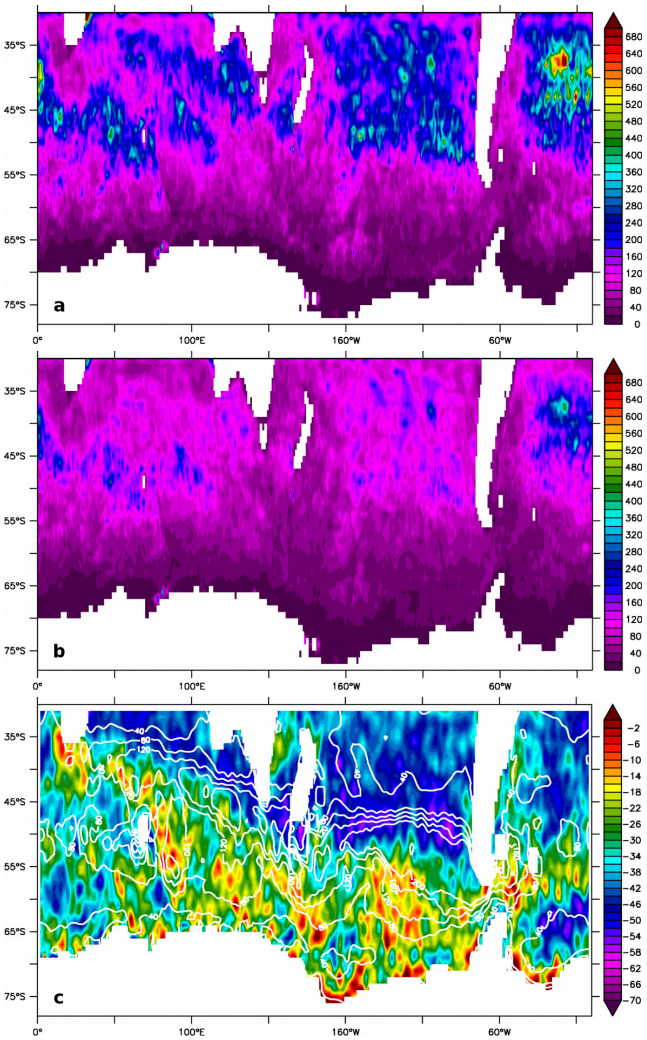

Figure 2. (a) CONTROL-GCM and (b) SVD-GCM time-averaged NIE integrated over the mixed layer (in Jm^{-2}) for the whole year 2001. (c) Relative difference of the two (in %), as defined in (8), together with the time-averaged mixed-layer depth as contour lines (contour interval 40 m).

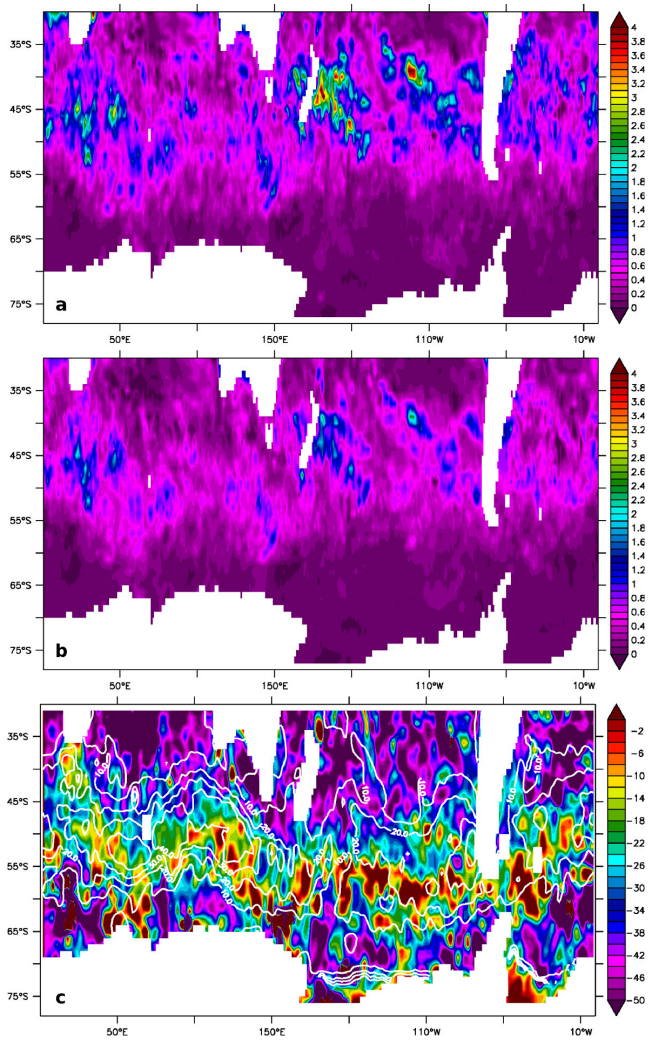

Figure 3. (a) CONTROL-GCM and (b) SVD-GCM time-averaged WPI into the near-inertial frequency band (in mWm^{-2}) for January 2001. (c) Relative difference of the two (in %), as defined in (9), together with the 10, 20, 30, and 40 m contour lines of time-averaged mixed-layer depth.

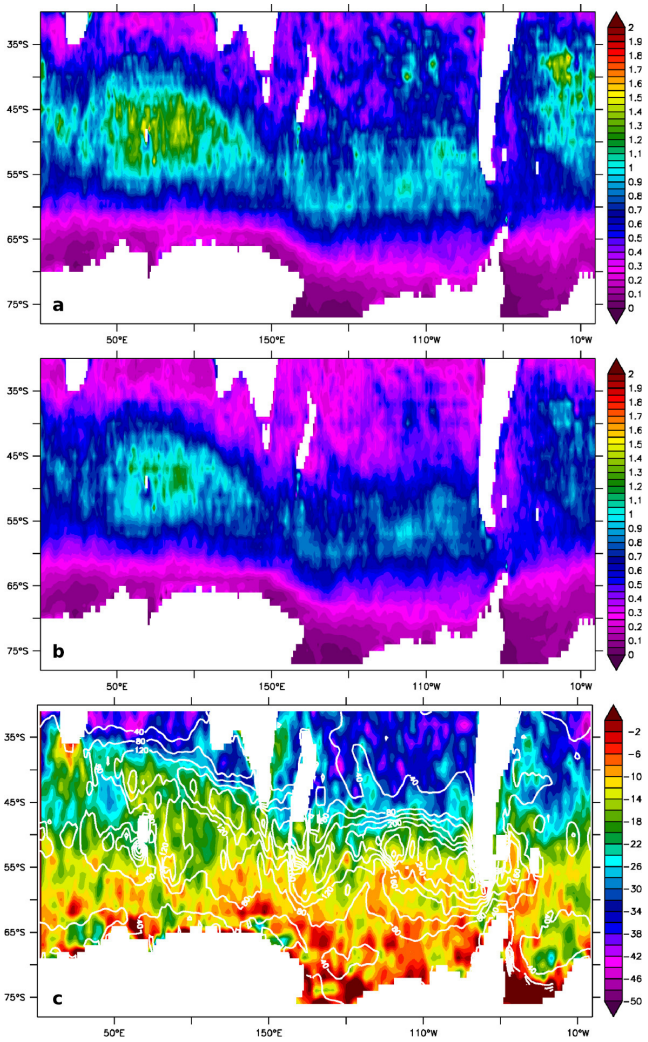

Figure 4. (a) CONTROL-GCM and (b) SVD-GCM time-averaged WPI into the near-inertial frequency band (in mWm^{-2}) for the whole year 2001. (c) Relative difference of the two (in %), as defined in (8), together with the mixed-layer depth as contour lines (contour interval 40 m).

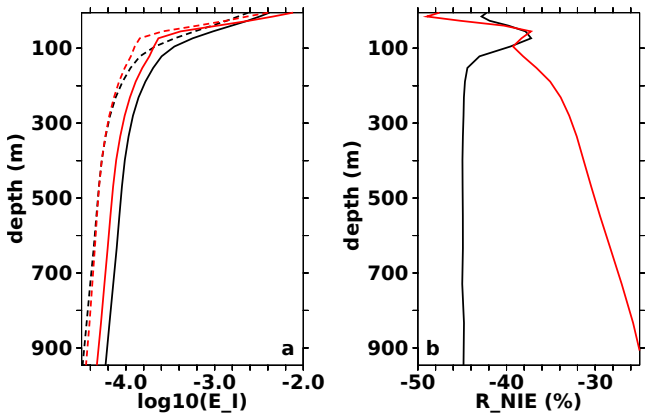

Figure 5. (a) $\log_{10}$ of horizontally and temporally averaged NIE (whole model domain) for January 2001 (red) and for the whole year 2001 (black). The solid lines show NIE for the run CONTROL-GCM and the dashed lines show NIE for the run SVD-GCM. (b) Relative difference of horizontally and temporally averaged NIE for January 2001 (red) and for the whole year 2001 (black).

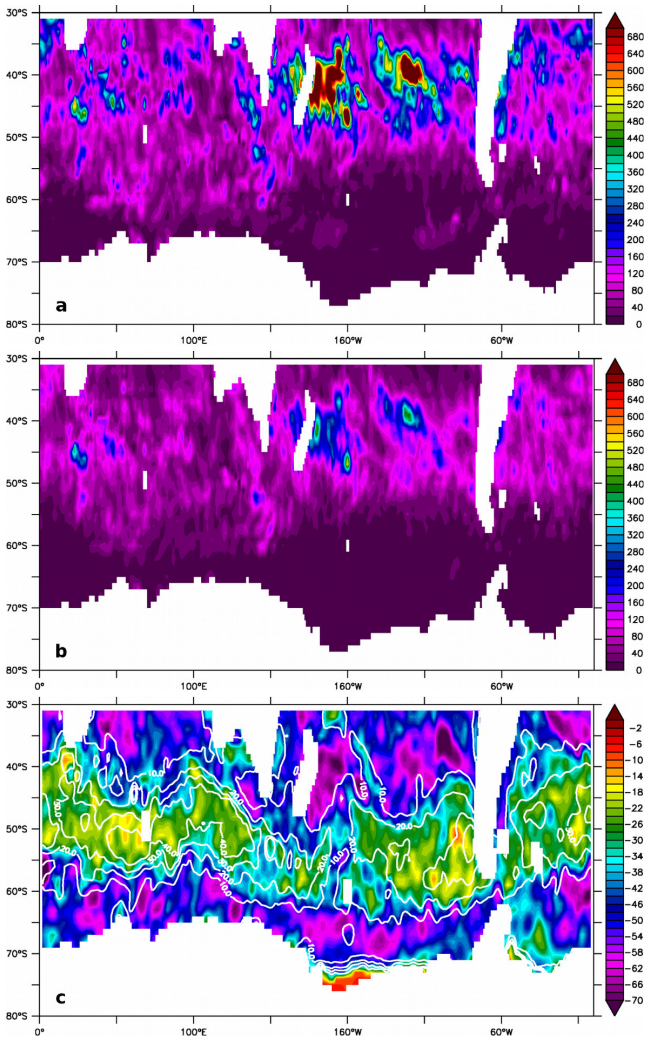

Figure 6. (a) CONTROL-SLAB and (b) SVD-SLAB time-averaged NIE integrated over the mixed layer (in Jm^{-2}) for January 2001. (c) Relative difference of the two (in %), as defined in (8), together with the 10, 20, 30, and 40 m contour lines of time-averaged mixed-layer depth.

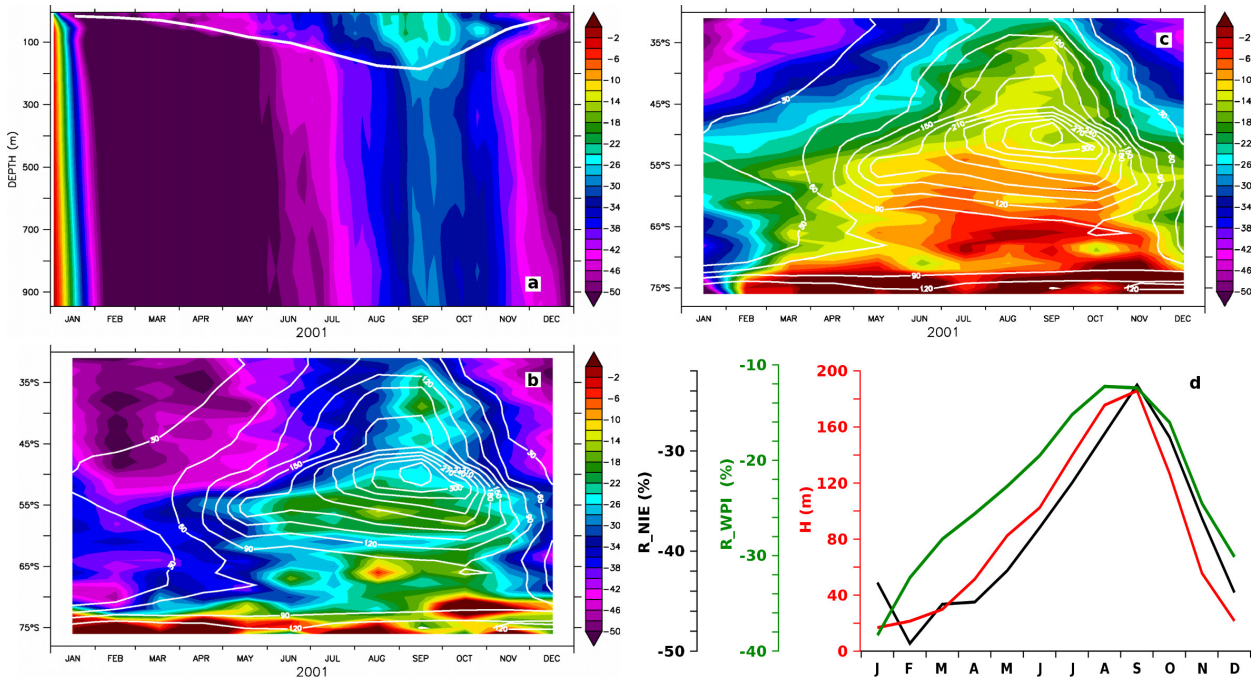

Figure 7. (a) Relative difference of horizontally averaged NIE in the mixed layer (colors) together with the horizontally averaged mixed-layer depth (white contour). (b) Relative reduction of zonally averaged NIE in the mixed layer (colors) together with the zonally averaged mixed-layer depth (contours every 30 m). (c) Relative reduction of zonally averaged near-inertial WPI (colors) together with the zonally averaged mixed-layer depth (contours every 30 m). (d) Relative reduction of horizontally averaged NIE in the mixed layer (black line) and relative reduction of horizontally averaged near-inertial WPI (green line) together with the horizontally averaged mixed-layer depth (red line). Relative differences are all given as defined in (8) and (9) in percent.

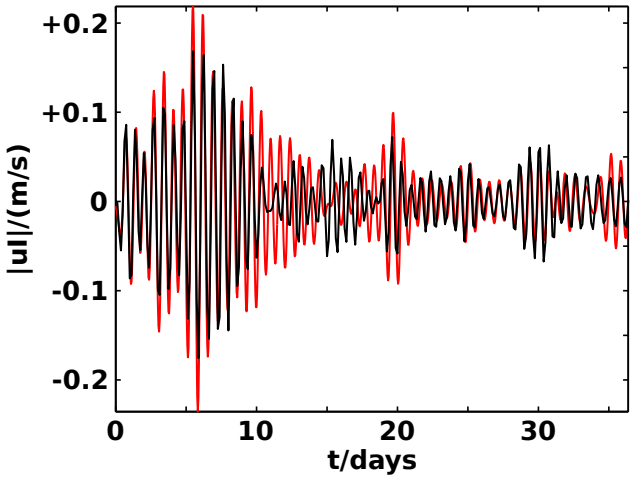

Figure 8. Zonal near-inertial velocity at $100°E$ and $45°S$. The black line shows u_I averaged over the mixed layer for the first 36.5 days of the experiment CONTROL-GCM and the red line shows u_I as modeled by PM70 using the same wind forcing, mixed-layer depth $H = 36.1$ m and $\epsilon = 4.5$ days.